UC San Diego
UC San Diego Previously Published Works

Title

Atmosphere teleconnections from abatement of China aerosol emissions exacerbate Northeast Pacific warm blob events.

Permalink

Journal

Authors

Wang, Hai
Zheng, Xiao-Tong
Cai, Wenju
et al.

Publication Date

DOI

Atmosphere teleconnections from abatement of China aerosol emissions exacerbate Northeast Pacific warm blob events

Hai Wang[a] , Xiao-Tong Zheng[a,1] , Wenju Cai[a,b,c] , Zi-Wen Han[a] , Shang-Ping Xie[d] , Sarah M. Kang[e] , Yu-Fan Geng[a], Fukai Liu[a] , Chuan-Yang Wang[a] , Yue Wu[a], Baoqiang Xiang[f,g] , and Lei Zhou[h,i]

During 2010 to 2020, Northeast Pacific (NEP) sea surface temperature (SST) experienced the warmest decade ever recorded, manifested in several extreme marine heatwaves, referred to as "warm blob" events, which severely affect marine ecosystems and extreme weather along the west coast of North America. While year-to-year internal climate variability has been suggested as a cause of individual events, the causes of the continuous dramatic NEP SST warming remain elusive. Here, we show that other than the greenhouse gas (GHG) forcing, rapid aerosol abatement in China over the period likely plays an important role. Anomalous tropospheric warming induced by declining aerosols in China generated atmospheric teleconnections from East Asia to the NEP, featuring an intensified and southward-shifted Aleutian Low. The associated atmospheric circulation anomaly weakens the climatological westerlies in the NEP and warms the SST there by suppressing the evaporative cooling. The aerosol-induced mean warming of the NEP SST, along with internal climate variability and the GHG-induced warming, made the warm blob events more frequent and intense during 2010 to 2020. As anthropogenic aerosol emissions continue to decrease, there is likely to be an increase in NEP warm blob events, disproportionately large beyond the direct radiative effects.

warm blob | aerosol forcing | atmospheric teleconnection

Since the 2010 s, multiple record-breaking warm sea surface temperature (SST) events (also known as warm blobs or marine heatwaves) have occurred in the Northeast Pacific (NEP). These events have had severe impacts on marine ecosystems (1–3), including biodiversity and the provision of ecosystem services (4), habitat compression of coastal upwelling and forage redistribution (5), and a coastwide toxic algal bloom along the North America west coast (6). In addition, such events have brought losses of billions of US dollars with widespread socioeconomic impacts (7). For example, the highly impactful California drought accompanied by the NEP warm blob events (8, 9) during 2013 to 2016 led to multibillion US dollars in agricultural losses (10–12) and the death of more than 100 million trees (13). These severe ecological and social consequences indicate the urgency of revealing the causes of these emerging climatic extremes.

The mechanisms underlying the recent dramatic NEP SST warming remain ambiguous. Previous studies have linked the NEP SST warm blob events to internal atmospheric variability associated with the North Pacific oscillation (NPO), El Niño and Southern oscillation (ENSO)-linked atmospheric forcing, and the Pacific decadal oscillation (PDO) (14–16). The NPO-like sea level pressure (SLP) pattern with a high-pressure (low-pressure) anomaly over the high-latitude (low-latitude) NEP acts to reduce surface winds, further reducing local evaporative cooling as well as wind-driven upper ocean mixing, resulting in strong NEP SST warming (8, 17, 18). The positive SST anomaly initiates positive thermodynamic feedback between the ocean and atmosphere through the wind-evaporation-SST (WES) feedback (19) and activates meridional modes (20), leading to the propagation of SST anomalies from the subtropics to the central equatorial Pacific and generating El Niño (21). Anomalous tropical convection due to El Niño induces atmospheric teleconnection to the extratropics, leading to the strengthening of the Aleutian Low and driving the oceanic expression of the positive PDO (22), reinforcing the NEP SST warm blob (15). Furthermore, the NEP SST warming reduces lower tropospheric stability, thereby decreasing low cloud cover and amplifying the NEP SST warming through the positive cloud-radiative-SST feedback (23), which played an important role in the summer 2019 warm blob event (24).

In addition to internal variability, greenhouse gas (GHG)-induced mean ocean warming may also contribute to an increase in marine heatwaves globally (25, 26), including in the NEP region. Anthropogenic aerosol emission is another important driver of climate change, which has offset a considerable portion of the GHG-induced warming (27) and

Significance

The period of 2010 to 2020 has witnessed the warmest Northeast Pacific (NEP) sea surface temperatures ever recorded, with several prolonged extreme ocean warming events. Though year-to-year internal climate variability may partially explain the appearance of these events, why they occurred dramatically more frequent remains elusive. We find that the rapid aerosol abatement in China triggers atmospheric circulation anomalies beyond its source region, driving a substantial mean surface warming in the NEP, which provides a favorable condition for extreme ocean warming events. Our findings provide an important insight into the mechanisms of the North Pacific ocean-atmosphere changes, highlighting the need to consider the exacerbated risks arising from a reduction in anthropogenic aerosol emissions in assessment of climate change impacts.

induced a north–south interhemisphere asymmetric SST response pattern (28). Specifically, the increased aerosol emissions from the Northern Hemisphere may contribute to the global warming hiatus and the associated negative PDO prior to 2012 (29, 30), albeit the aerosol's effect is weaker than that of GHG, and its influence on PDO is debatable (31, 32).

Given that internal variability regulates SST periodically and the GHG-induced warming has been ongoing for decades, the abrupt and conspicuous NEP SST warming in the last decade or so (Fig. 1) is unexpected. More importantly, aerosol emissions have substantial spatial and temporal changes that may have contributed to the recent NEP warming. In particular, since the 2010 s, aerosol emissions over East Asia have declined as a result of China's Clean Air Act (33, 34), leading to a greater local enhancement in precipitation (35, 36). It remains unclear to what extent the recent NEP SST warming is related to the concurrent decline in China aerosol emissions. Here, we show that the aerosol abatement in China causes localized tropospheric warming and induces atmospheric teleconnection from East Asia to the NEP with an intensified and southward-shifted Aleutian Low, reinforcing the recent
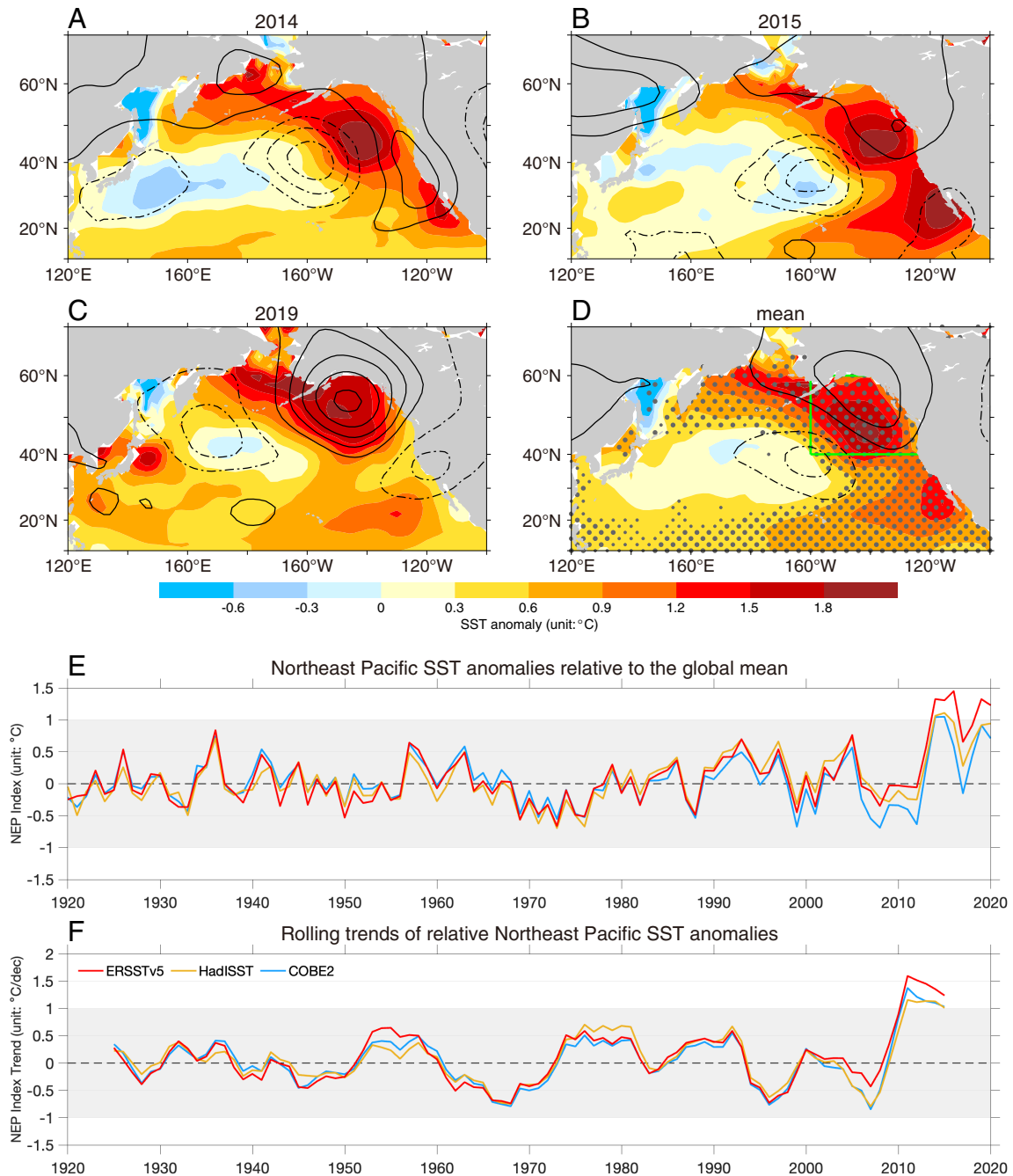
Fig. 1. Observed NEP SST warming and the corresponding atmospheric circulation anomalies. (*A–C*) The annual mean relative (referenced to the global mean SST) SST anomalies of 2014, 2015, and 2019, based on ERSSTv5 (shadings, in °C), and 500 hPa stream-function anomalies based on ERA5 (contours, in m² s⁻¹, 1 × 10⁶ m² s⁻¹ contour interval with 0 line omitted, solid contours denote clockwise circulation anomalies and dashed contours denote anticlockwise circulation anomalies). (*D*) The mean of the 2014, 2015, and 2019 relative SST and 500 hPa stream-function anomalies, with dots represent the mean relative SST anomalies are significant above the 95% (bigger dots) and 90% (smaller dots) CI based on Student's *t* test. (*E*) Time series of the annual mean NEP indices (in °C) during 1920 to 2020 in ERSSTv5 (red), HadISST (yellow), and COBE2 (blue). The NEP Index is defined as the regional mean relative SST anomaly averaged over the box of 160°W-120°W, 40°N-60°N (green box in *D*). (*F*) Time series of rolling 11-y trends of the annual mean NEP indices (in °C decade⁻¹) during 1920 to 2020 in ERSSTv5 (red), HadISST (yellow), and COBE2 (blue). The climatology is constructed over the 1950 to 2000 period.

rapid NEP SST warming through WES feedback and contributing to increased warm blob events beyond warming from the associated direct radiative effect.

Results

Observed Extraordinary NEP SST Warming. We investigate relative North Pacific SST anomalies referenced to global mean SST changes (*Detection and Attribution Analysis*) since in no other time in the recent history has there been a comparable rise in global mean temperature due to the increase in GHG concentration. The annual mean relative North Pacific SST anomalies in 2014, 2015, and 2019 show robust warming centers in the NEP after the global mean SST anomalies have been removed (Fig. 1 *A–C*), resembling the patterns of prominent warm blob events (15, 24). The mean of the relative SST anomalies of the three warm blob events features robust warming along the Bering Strait, Gulf of Alaska, and throughout the west coast of North America to low latitudes (Fig. 1*D*), with the warming center located in the NEP. Previous studies highlighted the importance of atmospheric forcing in driving the NEP SST warming (37) and the warm blob events (17, 38). The NPO-like north–south dipole anomalies of the 500 hPa stream-function reduce the climatological westerlies in the NEP (contours in Fig. 1 *A–D*), hence the evaporative cooling through the WES feedback, leading to the warm NEP SST anomaly.

To quantify the strength of the NEP SST warming over a longer period, we define a NEP Index (*Detection and Attribution Analysis*) as the regional mean relative SST anomaly that is centered around the significant NEP warming (green box in Fig. 1*D*). Except for the abovementioned events, the NEP Index is relatively stable throughout the entire 20th century, with changes between –1 °C and 1 °C and no robust warming trend (Fig. 1*E*). We calculate 11-y rolling trends of the NEP Index (Fig. 1*F* and *Detection and Attribution Analysis*). Results indicate that the rolling relative NEP warming trends never exceed 1 °C decade^{-1} in the 20th century, but show a rapid increase after 2007, and reach ~1.5 °C decade^{-1} in the very recent decade.

Given that the meridional dipole SST pattern in the North Pacific related to the PDO and ENSO is favorable for the warm blob events (15, 24), we remove the PDO- and ENSO-related SST anomalies (*Detection and Attribution Analysis*) from the original SST fields and calculate the North Pacific relative SST anomalies in 2014, 2015, and 2019, as well as the corresponding NEP Index during 1920 to 2020 (*SI Appendix*, Fig. S1). The residual SST anomalies in the North Pacific resemble those warm blob events (*SI Appendix*, Fig. S1 *A–D*). The magnitude of the relative NEP SST warming is ~0.75 °C (*SI Appendix*, Fig. S1*E*), more than half of that in the original fields (~1.4 °C) with the PDO and ENSO signals (Fig. 1*E*). Importantly, these recurring patterns due to internal climate variability cannot explain the dramatic NEP SST warming in the recent decade.

Furthermore, as variation in atmospheric circulation is a key factor in controlling the North Pacific SST anomalies (14, 17, 37, 38), we also examine the atmospheric circulation change during 1950 to 2020 by using empirical orthogonal function (EOF) analysis (*Detection and Attribution Analysis*) on the North Pacific SLP and investigate the associated SST pattern by regressing the North Pacific SST onto the principal components (PCs). The first and second EOF modes show the PDO and the NPO pattern, respectively. The PDO modulates the North Pacific SST and atmospheric circulation anomalies with its decadal signal, and the phase transition after 2010 may contribute to the NEP SST warming (*SI Appendix*, Fig. S2 *A* and *C*). The NPO contributes to the NEP SST anomalies by modulating surface heat flux changes through

intensifying (weakening) the climatological westerlies in their positive (negative) phase (*SI Appendix*, Fig. S2*B*). However, the NPO shows large interannual variations (*SI Appendix*, Fig. S2*D*) and hence is unlikely responsible for the recent rapid NEP SST warming.

We perform an EOF analysis on the low-frequency North Pacific SST (*SI Appendix*, Fig. S3 and *Detection and Attribution Analysis*) to distinguish the role of internal variability from external forcing at longer time scales. The leading PC1 features a continuous warming trend in the North Pacific SST, due primarily to external forcings (*SI Appendix*, Fig. S3 *A* and *C*). The second mode (PC2) correlates with the PDO index at 0.97, reflecting the low-frequency internal variability (*SI Appendix*, Fig. S3 *B* and *C*). The NEP SST anomalies show positive (negative) trends during a PDO warm (cold) phase, highlighting the role of the low-frequency PDO in modulating the NEP SST changes (*SI Appendix*, Fig. S3 *C* and *D*). Correlation between the low-frequency NEP Index and the sum of PC1 and PC2 is 0.80, suggesting that low-frequency NEP SST variability is driven by both external forcing and internal variability (*SI Appendix*, Fig. S3*D*).

Atmospheric GHG concentrations, as the major external forcing of the climate system, have increased steadily since the latter half of the 20th century, leading to the continuous warming of the global ocean. The PDO, as a robust recurring pattern of decadal climate variability in the extratropical North Pacific (39, 40), also contributes to the low-frequency change in the NEP SST (41, 42) (*SI Appendix*, Fig. S3*D*). After 2010, the negative-to-positive phase transition of the PDO and the GHG forcing partially explain the NEP SST warming, but the NEP has never experienced such rapid and substantial warming in any other historical period. The abrupt increase in PC1 after the 2010 s (*SI Appendix*, Fig. S3*C*) suggests that the dynamics underpinning the sudden NEP SST warming likely include external forcings beyond GHG emissions. Below, we show that reduced emissions of aerosols in China likely play an important role.

Reduced East Asia Aerosols. In contrast to the well-mixed GHGs, aerosol emissions are constantly evolving in space due to their short atmospheric residence time. Before 2007, both the aerosol emissions in East Asia and the global CO_2 concentration (Fig. 2*A*) showed a monotonic increase. Since 2014, global CO_2 levels have continued to rise sharply, but aerosol emissions from East Asia (mainly from China) have declined rapidly due to the implementation of China's Action Plan on the Prevention and Control of Air Pollution (Fig. 2 *A* and *B*). Other aerosol emission centers (i.e., South Asia, Europe, and North America, boxes in Fig. 2*B*) showed monotonic trends in the 21st century (*SI Appendix*, Fig. S4). We examine whether the reduction in aerosol emissions in East Asia affects the rapid SST warming in the NEP.

Unmasking of Warming in All-Forcing Experiments. We use 12 climate models from the same institution that participate both the phases 5 (CMIP5) (43) and 6 (CMIP6) (44, 45) of the Coupled Model Intercomparison Project (*SI Appendix*, Table S1). These simulations include "All forcing" agents subject to historical emissions and natural forcings (1850 to 2005 in CMIP5; 1850 to 2014 in CMIP6) for past climate change. We extend these data to 2020 by the Representative Concentration Pathway (RCP) 4.5 emission scenario in CMIP5 and by the shared socioeconomic pathway (SSP) 2-4.5 (SSP2-4.5) emission scenario in CMIP6, respectively. The GHG effects are similar in these simulations. However, they include a range of aerosol pathways. The CMIP6 models simulate the observed rapid reduction in aerosol emissions from East Asia during 2007 to 2020 (Fig. 2*A*); in contrast, the
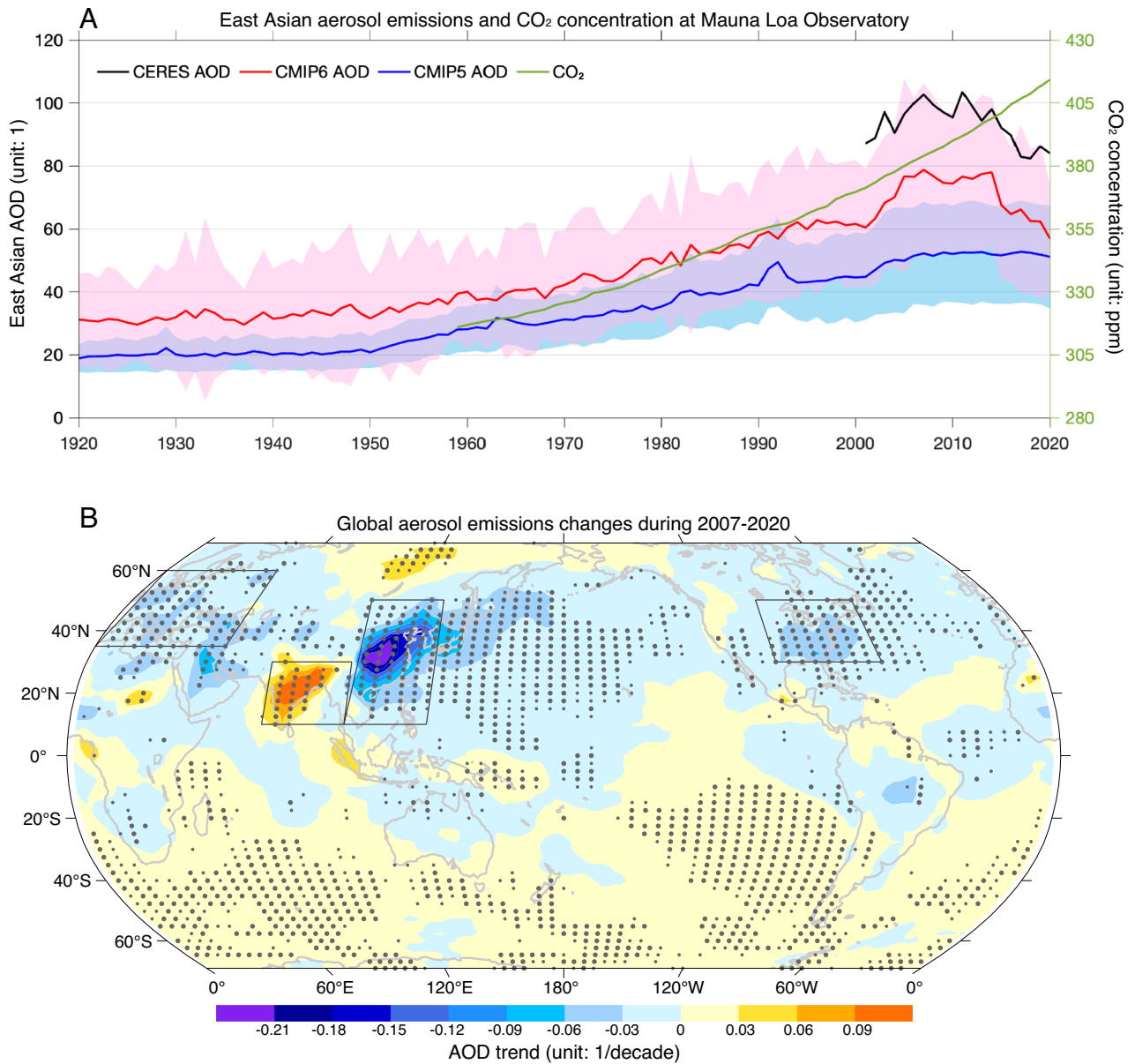
Fig. 2. Observed and simulated rapid changes of aerosol emissions in East Asia. (*A*) East Asian regional annual mean 550 nm AOD accumulations (in 1) in the observations (black) during 2001 to 2020, the CMIP6 All-forcing simulations extended using simulations under the SSP2-4.5 scenario (red), and the CMIP5 All-forcing simulations extended using simulations under the RCP4.5 scenario (blue) during 1920 to 2020. Lines are the multimodel ensemble means, and shadings represent the intermodel spreads with 1.0 SD. Green line denotes the observed CO_2 concentration (in parts per million) at Mauna Loa Observatory (1958 to 2020), Hawaii. (*B*) The annual mean 550 nm AOD trend (in 1 decade^{-1}) during 2007 to 2020 in the observations, with gray dots represent the trends are significant above the 95% (bigger dots) and 90% (smaller dots) CI based on Student's *t* test. Boxes are the ranges of regional mean 550 nm AOD accumulations in East Asia (100°E-130°E, 10°N-50°N), South Asia (70°E-100°E, 10°N-30°N), Europe (0°-50°E, 35°N-60°N), and North America (100°W-60°W, 30°N-50°N).

CMIP5 models are forced by East Asian aerosol emissions that flattened after the 2000 s, without incorporating a reduction in aerosol emissions in East Asia (Fig. 2*A*).

To remove the influence of differences in climate sensitivity in climate models, we normalize the SST and SLP trends during 1920 to 2006 and 2007 to 2020 by their global mean surface temperature change during 1950 to 2000 in each model and conduct the multimodel ensemble mean (MMEM) to examine the SST and atmospheric circulation responses between CMIP6 and CMIP5 All-forcing simulations. Prior to 2006, the CMIP6 and CMIP5 MMEMs show similar North Pacific SST changes, with a maximum warming in the Bering Sea at 0.3 ~ 0.4 °C decade^{-1} °C^{-1} and minimum warming in the mid-latitude North Pacific (*SI Appendix*, Fig. S5 *A* and *B*). Their difference in the North Pacific is small (*SI Appendix*, Fig. S5*C*). The

regional mean normalized NEP SST anomalies during 1920 to 2006 in CMIP6 and CMIP5 are both ~0.05 °C decade^{-1} °C^{-1}. Thus, CMIP6 and CMIP5 simulate comparable externally forced changes in the North Pacific SST during 1920 to 2006.

By contrast, during 2007 to 2020, the CMIP6 MMEM shows marked North Pacific warming centered in the NEP (Fig. 3*A*), with a regional mean NEP SST anomaly at 0.93 °C decade^{-1} °C^{-1}. However, the North Pacific SST trend during 2007 to 2020 in CMIP5 is quite different, showing a warming in the mid-latitude North Pacific and a weak response in the NEP (Fig. 3*B*), with 0.22 °C decade^{-1} °C^{-1} of the regional mean NEP SST anomaly. More importantly, the difference in the North Pacific warming pattern between CMIP6 and CMIP5 shows a conspicuous NEP SST warming centered from the Bering Strait to the Gulf of
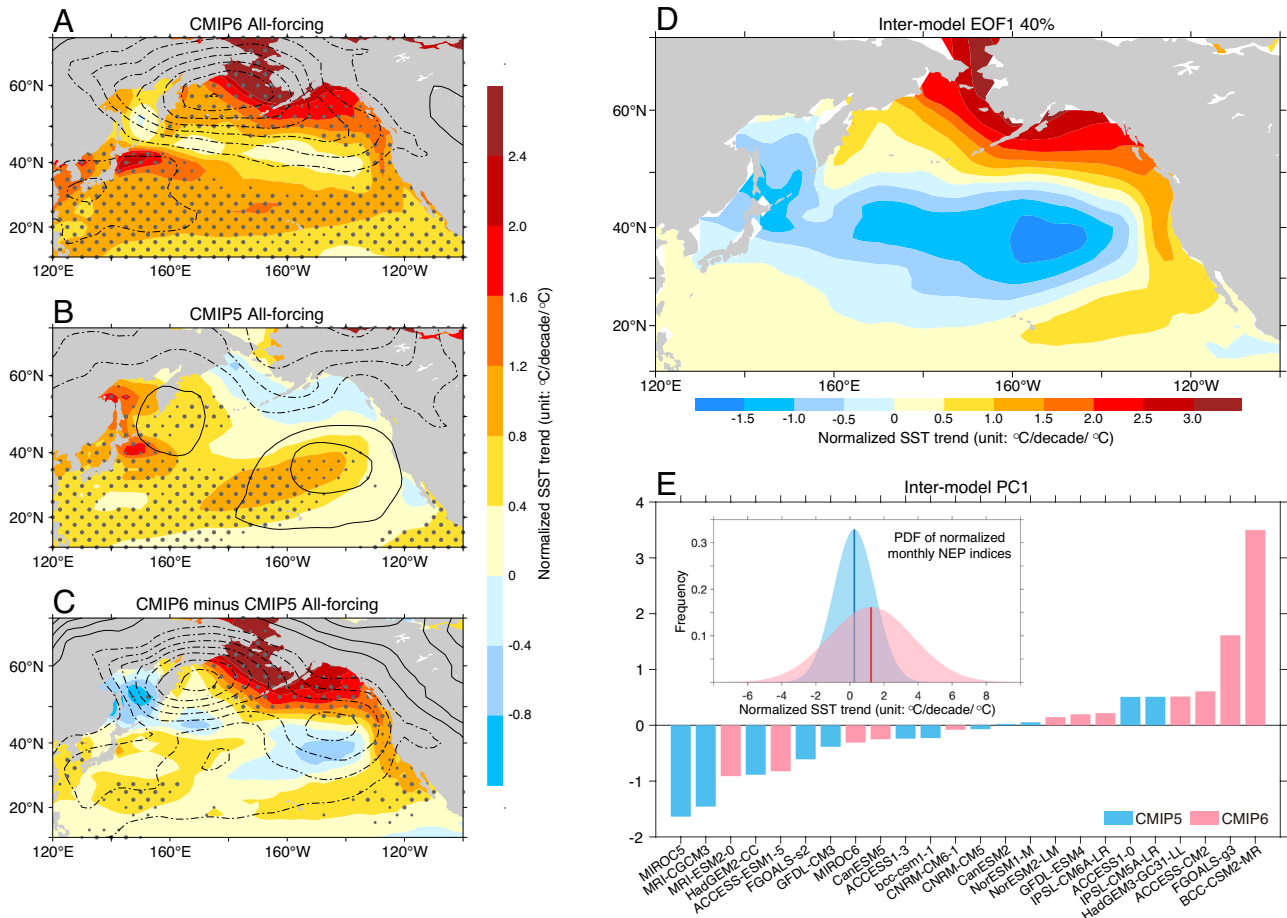
Fig. 3. Declined East Asian aerosol emissions induced North Pacific SST and SLP changes in CMIP6 and CMIP5 All-forcing simulations. (*A*) The normalized (by global mean surface temperature change during 1950 to 2000) annual mean SST (shadings, in °C decade^{-1} °C^{-1}) and SLP (contours, in hPa decade^{-1} °C^{-1}, 0.5 hPa decade^{-1} °C^{-1} contour interval with 0 line omitted, solid contours denote high-pressure anomalies and dashed contours denote low-pressure anomalies) trends during 2007 to 2020 in the CMIP6 All-forcing simulations extended using simulations under the SSP2-4.5 scenario. (*B*) Same as *A* but for the CMIP5 All-forcing simulations extended using simulations under the RCP4.5 scenario. (*C*) Differences between *A* and *B*. The gray dots represent the normalized SST trends are significant above the 95% (bigger dots) and 90% (smaller dots) CI among different climate models based on Student's *t* test. (*D* and *E*) The first intermodel EOF mode (shadings, in °C decade^{-1} °C^{-1}) and the corresponding PC of the normalized SST trends during 2007 to 2020 in 12 CMIP6 models (pink bars) and 12 CMIP5 models (blue bars). The explained variance is reported on the *Top* of the panel. Subplot in *E* denotes the probability density functions of the normalized monthly NEP SST trends during 2007 to 2020 in 12 CMIP6 models (pink, red line denotes the mean value: 1.24 °C decade^{-1} °C^{-1}) and 12 CMIP5 models (blue, blue line denotes the mean value: 0.26 °C decade^{-1} °C^{-1}).

Alaska, extending throughout the west coast of North America to low latitudes (Fig. 3*C*), resembling the observed NEP warming pattern during the blob events (Fig. 1*D*). The corresponding atmospheric circulation shows an intensified and southward-shifted Aleutian Low with negative SLP anomalies centered to the southwest of the Bering Strait in CMIP6, which is manifested in the difference between CMIP6 and CMIP5 results (contours in Fig. 3 *A* and *C*). This anomalous SLP pattern and the corresponding surface wind anomalies warm the NEP SST by suppressing the evaporative cooling through WES feedback.

We evaluate the intermodel differences in SST changes by applying EOF analysis on the normalized SST trends over the 2007 to 2020 period in the 24 models. The leading EOF mode (40.0% explained variance) captures the pronounced North Pacific warming pattern, resembling the NEP SST warming in both the observations and MMEM results (Fig. 3*D*). The corresponding intermodel differences in the intensity of the warming pattern are reflected in the PC values (bars in Fig. 3*E*). Overall, the intensity of the warming pattern in CMIP6 (red bars), with decreasing East Asia aerosols, is larger than that in CMIP5 (blue bars) with flattened East Asia aerosols.

Because the GHG effects are similar between the CMIP6 and CMIP5 models, and internal variability, whose phase varies

randomly across models, is largely removed in the MMEM, the warming signals in each MMEM warming pattern are mostly externally forced. The results indicate that the mean warming of the NEP SST due to the rapid reduction in aerosol emissions in East Asia during 2007 to 2020 likely plays an important role in the formation of the observed NEP SST warm blob events, as captured by the CMIP6 models but absent in the CMIP5 models.

Using normalized monthly NEP SST trends during 2007 to 2020 in each of the 12 CMIP6 and 12 CMIP5 models, we construct two probability density functions. Their comparison shows a warmer NEP SST in CMIP6 (mean value: 1.24 °C decade^{-1} °C^{-1}) than that in CMIP5 (mean value: 0.26 °C decade^{-1} °C^{-1}) All-forcing simulations (Fig. 3*E*), translating into an increased frequency of samples with high SST anomalies. For example, using a threshold value of 2.0 °C decade^{-1} °C^{-1} warming, the frequency increases from 8% in CMIP5 with leveled East Asian aerosols to 38% in CMIP6 with decreased East Asian aerosols.

Unmasking of Warming in Single-Forcing Experiments. In addition to the All-forcing simulations in CMIP6 and CMIP5, we use the latest simulations from the Detection and Attribution Model Intercomparison Project in the CMIP6 dataset (*SI Appendix, Table S1*) to isolate the role of individual forcing in shaping the North

Pacific SST responses. We use the same 12 models as in CMIP6 All-forcing simulations that performed the historical anthropogenic aerosol or GHG only single-forcing simulations during 1850 to 2020. In the single-forcing simulations, anthropogenic aerosols or GHGs are the only time-varying forcing agent, while the other forcings are fixed at the preindustrial level.

Comparison of EOF analysis on the low-frequency North Pacific SST changes during 1920 to 2020 between CMIP6 All-forcing and single-forcing simulations (Fig. 4 and *Detection and Attribution Analysis*) highlights the role of aerosol-forcing in modulating the NEP SST anomalies. The leading PC denotes the long-term change in the external forcing signals; the variance contributions in All-forcing, Aerosol-forcing, and GHG-forcing simulations are 94.2%, 93.4%, and 97.8%, respectively. In the All-forcing and GHG-forcing simulations, the NEP SST shows continuous warming (Fig. 4 *A*, *C*, and *D*). However, in the Aerosol-forcing simulations, a continuous cooling of the NEP SST persists until around 2007, thereafter a rapid warming trend is established when the East Asian aerosol emissions are reversed (Fig. 4 *B* and *D*).

Regressed SLP changes onto the PCs verify the role of atmospheric circulation changes in shaping the North Pacific SST responses (contours in Fig. 4 *A–C*). A comparison between the All-forcing and single-forcing simulations reinforces that the East Asian anthropogenic aerosol emission reduction dominates the NEP SST warming after 2007. By contrast, the GHG-forcing contributes but is not the primary cause of the rapid NEP SST warming after 2007.

Taking into account all the CMIP6 and CMIP5 All-forcing simulations, the CMIP6 anthropogenic aerosol, GHG, as well as natural single-forcing simulations, we find that the NEP indices reaffirm the role of the reversal in East Asian aerosol emissions in modulating the NEP SST anomaly. The reversal in aerosol emissions amplifies warming after 2007 as seen in the comparison between CMIP6 and

CMIP5 All-forcing simulations after 2007 (*SI Appendix*, Fig. S6*A*) and in CMIP6 historical anthropogenic aerosol single-forcing simulations (*SI Appendix*, Fig. S6*B*). The GHG single-forcing simulations produce a continuous warming in the NEP SST (*SI Appendix*, Fig. S6*C*), and the naturally forced experiments generate no persistent NEP SST changing (*SI Appendix*, Fig. S6*D*).

There are four main regions for aerosol emissions in the 20th century: East Asia, South Asia, Europe, and North America. To identify their relative importance, we regress the global 550 nm aerosol optical depth (AOD) anomalies onto the NEP Index in CMIP6 historical anthropogenic aerosol single-forcing simulations (*Detection and Attribution Analysis*) and find that the most significant AOD anomalies associated with the NEP SST changes are located in East Asia and to a less extent in South Asia. The aerosol emissions from Europe are also related to the NEP SST changes but with a relatively small magnitude (*SI Appendix*, Fig. S7).

Impact through Atmospheric Teleconnections. The reduced East Asian aerosol emissions lead to an intensification and southward-shift of the Aleutian Low and generate the NEP SST warming by atmospheric forcing. A tropospheric heating anomaly induced by East Asian aerosol emissions has been suggested to be an important mechanism affecting the North Pacific atmospheric circulation (29, 46).

We test this mechanism by conducting two sets of coupled climate model simulations with and without Chinese aerosol emissions using the Community Earth System Model Version 2 (CESM2) (47) (*CESM2 Experiments*). To isolate the climate effect of changes in aerosol emissions from China, all the other forcings are held constant at their 2000 level. The two sets of simulations differ only in China's SO_2 and black carbon (major aerosol species) aerosol emissions, one at their 2000 level as a control simulation (*CTRL*), and the other one with the SO_2 and black carbon aerosol emissions in China removed (*noCN*) (*SI Appendix*, Fig. S8). Each set of the
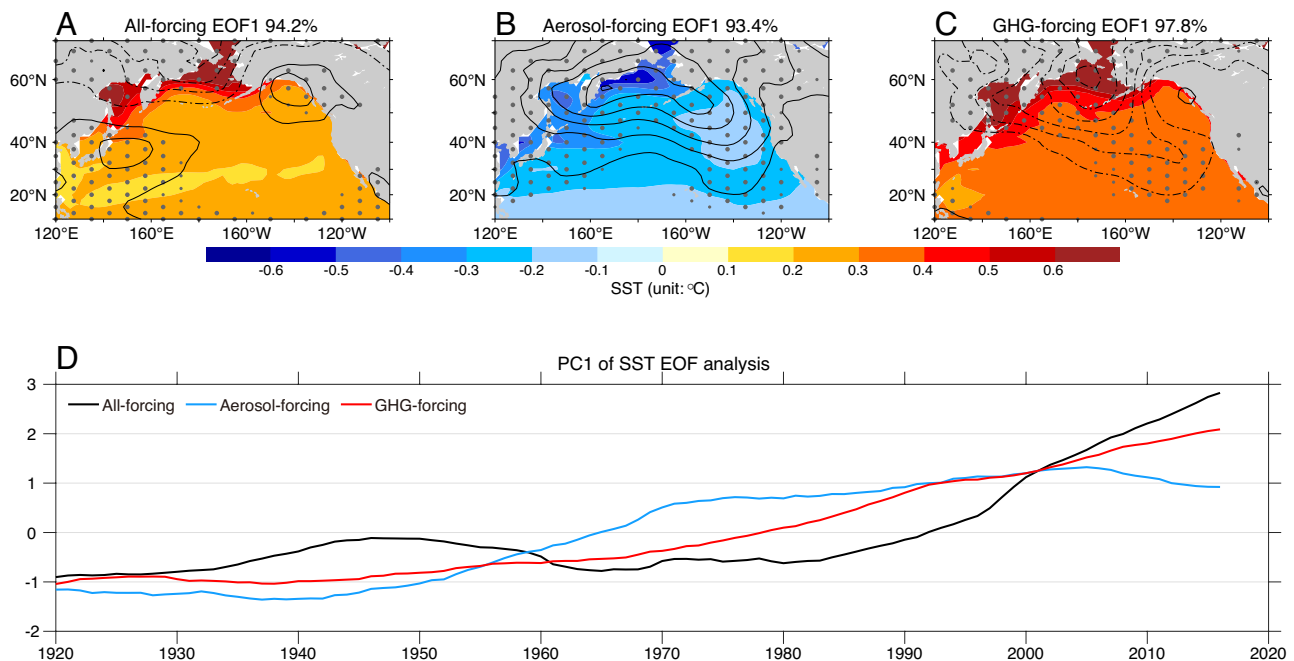

Fig. 4. Leading modes of externally forced North Pacific SST and SLP changes in CMIP6 simulations. (*A*) The first EOF mode of 9-y low-pass filtered annual mean SST anomaly (shadings, in °C) during 1920 to 2020 in CMIP6 All-forcing simulations extended using simulations under the SSP2-4.5 scenario. The explained variance is reported on the *Top* of the panel. (*B* and *C*) Same as *A* but for the anthropogenic aerosol single-forcing (*B*) and GHG single-forcing (*C*) simulations, respectively. Contours in *A–C* are the regressions of the North Pacific SLP onto the PC1 of the EOF analysis (in hPa per SD of the PC1, 0.05 hPa contour interval with 0 line omitted, solid contours denote high-pressure anomalies and dashed contours denote low-pressure anomalies). The gray dots represent the SLP regressions are significant above the 95% (bigger dots) and 90% (smaller dots) CI based on Student's *t* test. (*D*) The corresponding PCs of the EOF analysis. The climatology is constructed over the 1950 to 2000 period.

simulation is branched into a 10-member ensemble with slightly different perturbations in initial atmospheric states. The ensemble mean results can substantially remove the internal variability signal and represent the externally forced responses. Each ensemble member is run for 20 y. The global mean net radiative flux at the top of the atmosphere adjusts fast in the first 5 y (*SI Appendix*, Fig. S9). Therefore, we use the last 15-y mean as the response. The comparison between the *noCN* and *CTRL* simulations quantifies the

transient climate response (including the rapid NEP SST warming) by removing major aerosol emissions from China. The total equilibration of the deep ocean, which can take hundreds to thousands of years (48), is beyond the scope of the current study.

We find that the removal of SO_2 and black carbon aerosol emissions from China leads to a substantial decrease in AOD centered in East China (*SI Appendix*, Fig. S10A), resulting in an increase in the atmospheric absorbed solar flux (*SI Appendix*,
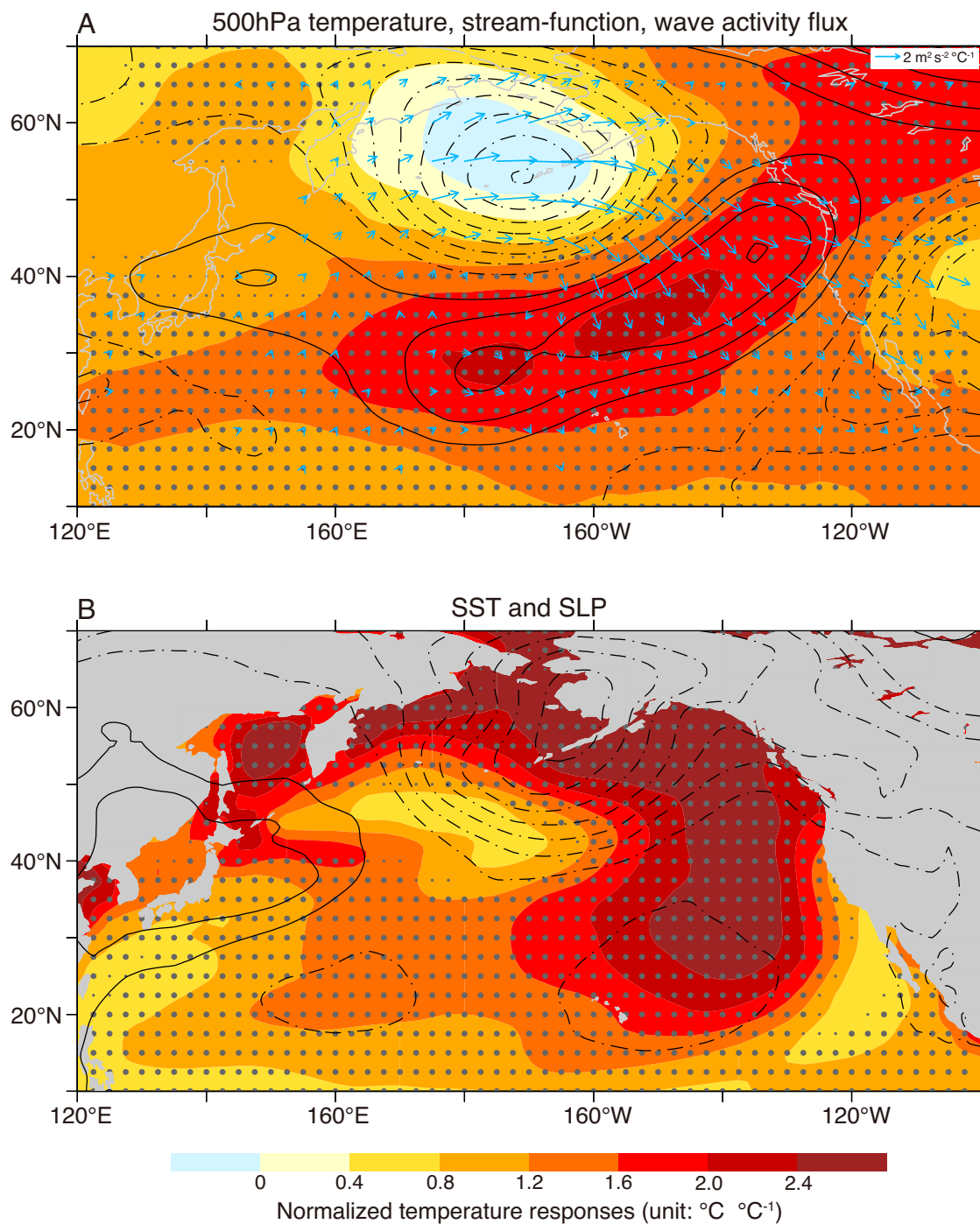
Fig. 5. Declined Chinese aerosol emissions induce NEP coupled ocean–atmosphere responses in the CESM2 experiments. Shown are responses normalized by global mean surface temperature response between the *noCN* and *CTRL* simulations. (*A*) Ensemble mean responses of annual mean 500 hPa atmospheric temperature (shadings, in °C °C⁻¹), stream-function (contours, in m² s⁻¹ °C⁻¹, 5 × 10⁵ m² s⁻¹ °C⁻¹ contour interval with 0 line omitted, solid contours denote clockwise circulation anomalies and dashed contours denote anticlockwise circulation anomalies), and wave-activity fluxes (vectors, in m² s⁻² °C⁻¹, scale on the *Top Right*, values smaller than 0.1 m² s⁻² °C⁻¹ omitted). (*B*) Same as *A* but for responses of SST (shadings, in °C °C⁻¹) and SLP (contours, in hPa °C⁻¹, 0.5 hPa °C⁻¹ contour interval with 0 line omitted, solid contours denote high-pressure anomalies and dashed contours denote low-pressure anomalies). The gray dots represent that the 500 hPa atmospheric temperature and SST responses are significant above the 95% (bigger dots) and 90% (smaller dots) CI based on Student's *t* test. All results were derived as the difference between the *noCN* and *CTRL* simulations.

Fig. S10*B*). In response to the atmospheric radiative heating anomaly, the 500 hPa atmospheric temperature increases in and along the downstream of the heating source due to advection by the climatological westerlies (Fig. 5*A*). The anomalous atmospheric warming induces alternating divergent and convergent flows as illustrated by the 500 hPa stream-function (contours in Fig. 5*A*), with wave-activity fluxes that signify the propagation of the atmospheric teleconnection pattern from the forcing center to the NEP (vectors in Fig. 5*A*).

As a part of the atmospheric teleconnection pattern, an intensified and southward-shifted Aleutian Low is induced, promoting the NEP SST warming through the WES feedback as the local climatological westerlies weaken (contours in Fig. 5*B*). The SST response shows a "horse-shoe" like warming pattern with warming from the Bering Strait to the Gulf of Alaska, extending throughout the west coast of North America to low latitudes (Fig. 5*B*). The atmospheric anomalies and the corresponding SST warming pattern in the CESM2 experiments resemble the differences between the CMIP6 and CMIP5 All-forcing simulations with and without Chinese aerosol reductions (Fig. 3*C*), providing pieces of evidence for a linkage between the Chinese aerosol cleanup and the NEP SST warming.

Discussion

The warm blob events are closely related to year-to-year internal climate variability. However, the internal climate variability cannot explain the abrupt continuous NEP SST warming in the most recent decade. The GHG-induced warming, which has been ongoing steadily for decades, is also not responsible for this specific NEP SST warming. We found an important role by China aerosol abatement in driving the rapid NEP SST warming, which provides favorable conditions for the warm blob events over the past decade. The rapid warming of the NEP SST is not simply due to the direct radiative effect of the declined China aerosol emissions; the reduced aerosol emissions also induce an atmospheric circulation response in the North Pacific via atmospheric teleconnections that weaken the surface winds over the region. This aerosol-induced North Pacific atmospheric circulation anomaly (Figs. 3*C* and 5) is different from that induced by internal climate variability (Fig. 1*D*) which directly leads to the warm blob events. The intensified and southward-shifted Aleutian Low from the aerosol reduction we emphasized in this study results in a conspicuous rapid mean NEP SST warming, along with internal climate variability and GHG forcing, leading to the frequent and intense warm blob events in the most recent decade.

Our findings thus provide an important advance in understanding and attributing the recent past climate change, relevant for assessing the probability of future warm blob events in the NEP. In the coming decades, radiative heating from a continued reduction in anthropogenic aerosol emissions will itself increases such events, and the heating will also triggers large-scale atmospheric teleconnections with far-reaching impacts on climate and society well beyond the aerosol source regions (34). One such impact is a substantial increase in NEP warm blob events, disproportionally large beyond the direct radiative effect, and dramatic when reinforced by other factors such as decadal variability (16), the GHG-induced North Pacific (49), and Arctic (50) warming.

Materials and Methods

The acronyms used in this paper are listed and explained in *SI Appendix*, Table S2.

Observations. We mainly use the National Oceanic and Atmospheric Administration Extended Reconstruction SST, version 5 (ERSSTv5) product (51) to evaluate the North Pacific SST changes. The data are available on a 2° × 2° horizontal grid globally for the period of 1854 to 2020. We also use the HadISST

(52) and COBE-SST2 (53) products for comparison. The observed monthly PDO index is taken from the National Centers for Environmental Information, National Oceanic and Atmospheric Administration for the period of 1920 to 2020. The El Niño index is defined as the detrended Niño3.4 index (5°S-5°N, 170°W-120°W regional mean SST anomaly). The associated atmospheric variables, including SLP and geopotential height, are taken from the fifth generation European Centre for Medium-Range Weather Forecasts atmospheric reanalysis (ERA5) (54) on a horizontal grid of 0.25° × 0.25°for the period of 1950 to 2020. The observed AOD at 550 nm wavelength is taken from the NASA Clouds and Earth's Radiant Energy System (CERES), which collects the Moderate Resolution Imaging Spectroradiometer/Visible Infrared Imaging Radiometer Suite aerosols (55). The data are available on a 1° × 1° horizontal grid globally for the period of 2001 to 2020. The CO_2 concentration at Mauna Loa Observatory is taken from the Scripps Institution of Oceanography, University of California San Diego for the period of 1958 to 2020 (56).

CMIP5 and CMIP6 Outputs. We use coupled climate model simulations from the phases 5 (CMIP5) (43) and 6 (CMIP6) (44, 45) of the Coupled Model Intercomparison Project (*SI Appendix*, Table S1). The CMIP5 historical simulations ended in 2005 and the CMIP6 historical simulations ended in 2014. Thus, we extend them to 2020 with RCP4.5 and SSP2-4.5 scenarios, respectively. The roles of distinct external forcing factors are estimated by using CMIP6 historical simulations singly forced by anthropogenic aerosols, GHGs, natural solar variations, and volcanic eruptions. The CMIP6 historical single-forcing simulations ended in 2020. The ensemble of CMIP6 analysis includes 12 climate models that performed the historical simulations, SSP2-4.5 simulations, and historical single-forcing simulations simultaneously with the same "realization", "initialization", "physics" and "forcing" sets. The ensemble of CMIP5 analysis includes 12 climate models from the same institutions as those in CMIP6. We use only the "r1" realization in each model to keep equal weight in the MMEM analysis. The effects of anthropogenic aerosol-forcing are diagnosed in two different ways: CMIP6 All-forcing (extended by SSP2-4.5) minus CMIP5 All-forcing (extended by RCP4.5) simulations, and CMIP6 historical anthropogenic aerosol single-forcing simulations. All model outputs are regridded to a 2.5° × 2.5° horizontal resolution.

Detection and Attribution Analysis. We analyze the annual mean anomalous relative SST referenced to the global mean SST anomalies and the 500 hPa stream-function in 2014, 2015, and 2019 in the observations and the mean of the above three NEP SST warm blob events. The significance of the observed mean relative SST is tested at 90% and 95% confidence levels with Student's *t* test. The NEP indices are calculated as the annual mean relative SST anomalies averaged over the box of 160°W-120°W, 40°N-60°N based on the range of the three pronounced NEP warm blob events as shown in Fig. 1. We also calculate 11-y rolling trends of the NEP Index (years in Fig. 1*F* indicate the middle years of the 11-y rolling windows). The NEP regional mean SST changes among the distinct PDO phases are evaluated by linear trends.

To analyze the influence of the PDO and ENSO on the NEP SST warming, we remove the PDO- (with annual mean PDO index) and ENSO- (with annual mean Niño3.4 index) related SST anomalies step-by-step through linear regression and calculate the relative SST anomalies as well as the NEP Index in the residual SST fields.

To diagnose the atmospheric forcing pattern in the North Pacific, the first two EOFs and PCs of the annual mean SLP anomaly over the North Pacific are computed during 1950 to 2020. Before the EOFs, the SLP is detrended to eliminate the long-term trend signal. To calculate the contributions from the PDO forcing and NPO forcing to the North Pacific SST anomalies, we use linear regressions projecting the SST anomaly over the North Pacific onto the PC1 and PC2 of the SLP EOF analysis, respectively. The significance of the regression analysis is also tested at 90% and 95% confidence levels with Student's *t* test. To evaluate the internal variability and the forced climate response from a long-term change perspective, we compute the first two EOFs and PCs of the low-frequency annual mean SST anomaly over the North Pacific during 1920 to 2020. Before the EOFs, a 9-y low-pass filter is applied to eliminate the high-frequency signals of the SST changes.

The regional annual mean 550 nm AOD changes are averaged over East Asia (100°E-130°E, 10°N-50°N), South Asia (70°E-100°E, 10°N-30°N), Europe (0°-50°E, 35°N-60°N), and North America (100°W-60°W, 30°N-50°N) based on observed and CMIP5/6 simulated aerosol concentration changes. Besides, the linear trend of 550 nm AOD during 2007 to 2020 is also calculated to show the

rapid reduction in East Asian aerosol emissions. Student's *t* test is used to estimate the 90% and 95% statistical significance of the trends.

In the climate model analysis, to minimize the climate sensitivity among different climate models, we calculate the normalized (by the 1950 to 2000 global mean surface temperature change in each model) SST and SLP trends during 1920 to 2006 and 2007 to 2020 in each of the CMIP6 and CMIP5 All-forcing models, respectively, and then conduct the MMEM analysis. The statistical significance of the normalized SST trends among different climate models is evaluated with Student's *t* test at 90% and 95% confidence levels. Besides, we apply an intermodel EOF analysis on the normalized SST trends during 2007 to 2020 among the different CMIP6 and CMIP5 All-forcing models to check the intermodel consistency. We also construct two probability density functions based on the normalized monthly NEP SST trends in each of the 12 CMIP6 and 12 CMIP5 models to examine the frequency of samples with high NEP SST anomalies.

To isolate the role of anthropogenic aerosol-forcing changes in shaping the North Pacific SST responses, we apply an EOF analysis on the 9-y low-pass filtered annual mean SST anomalies in CMIP6 All-forcing, anthropogenic aerosol single-forcing, and GHG single-forcing simulations during 1920 to 2020. The corresponding atmospheric circulation responses are evaluated by the regressions of the SLP to the PC1 of the EOF analysis and are tested based on Student's *t* test at 90% and 95% confidence levels. In addition, we calculate the NEP indices in the CMIP6 and CMIP5 All-forcing, and CMIP6 GHG, aerosol, natural single-forcing simulations along with their intermodel spreads to examine their long-term changes during 1920 to 2020. Regressions of the 550 nm AOD anomalies onto the NEP Index during 1920 to 2020 in the CMIP6 anthropogenic aerosol single-forcing simulations are carried out to examine the relative role of aerosol source regions. The statistical significance of this regression is tested to be above the 95% confidence level based on Student's *t* test.

Diagnosis of Aerosol-Induced Stationary Waves. The wave-activity flux is a locally applicable conservation relation that is derived for quasigeostrophic stationary waves on a zonal flow, a generalization of the Eliassen–Palm relation (57). It is a useful diagnostic tool for the three-dimensional propagation of stationary wave activity. By using the wave-activity flux, we can diagnose the atmospheric circulation anomaly and the corresponding stationary wave propagation along the mid-to-high latitudes North Pacific, which is driven by the aerosol emission changes in East Asia.

On the sphere, the nondivergent geostrophic wind velocities are:

$$\begin{cases} u = -\dfrac{1}{a}\dfrac{\partial \psi}{\partial \phi} \\ v = \dfrac{1}{a\cos\phi}\dfrac{\partial \psi}{\partial \lambda} \end{cases},$$

where the stream-function $\psi = \Phi / 2\Omega\sin\phi$, Φ is the geopotential and Ω is the Earth's rotation rate, a is the Earth's radius, and (ϕ, λ) are latitude and longitude, respectively. The stream-function is calculated at the 500 hPa level in this study. With the quasigeostrophic theory, the wave-activity flux F_s is calculated as follows (Eq. 5.7 in ref. 57):

$$F_s = p\cos\phi \begin{pmatrix} \dfrac{1}{2a^2\cos^2\phi}\left[\left(\dfrac{\partial \psi'}{\partial \lambda}\right)^2 - \psi'\dfrac{\partial^2 \psi'}{\partial \lambda^2}\right] \\ \dfrac{1}{2a^2\cos\phi}\left(\dfrac{\partial \psi'}{\partial \lambda}\dfrac{\partial \psi'}{\partial \phi} - \psi'\dfrac{\partial^2 \psi}{\partial \lambda\partial\phi}\right) \\ \dfrac{2\Omega^2\sin^2\phi}{N^2 a\cos\phi}\left(\dfrac{\partial \psi'}{\partial \lambda}\dfrac{\partial \psi'}{\partial z} - \psi'\dfrac{\partial^2 \psi}{\partial \lambda\partial z}\right) \end{pmatrix},$$

in which $p = \frac{pressure}{1000hPa}$, and the *pressure* is set to 500 hPa. $z = -H\ln p$, where *H* is a constant scaleheight, *N* is the buoyancy frequency, and ψ' is the perturbed change of 500 hPa stream-function. Detailed programs for calculation of wave-activity flux are available at http://www.atmos.rcast.u-tokyo.ac.jp/nishii/programs/index.html.

CESM2 Experiments. We use the CESM2 with a fully coupled atmosphere (Community Atmosphere Model version 6, CAM6), ocean (Parallel Ocean Program version 2), land (Community Land Model version 5), sea ice (Community Ice CodE version 5), and river (River Transport Model) components (47). The CAM6 atmosphere models involve interactive aerosol processes using Modal Aerosol Model version 4 (58). The atmosphere model runs on a nominal 2° horizontal grid with 32 vertical layers, and the ocean model is configured with a horizontal grid of 1° with 60 vertical layers ("f19_gx1v7" horizontal resolution).

Two sets of ensemble simulations (10 members for each case) are conducted to distinguish the climate response to the Chinese aerosol abatement. In the *CTRL*, we restart the model from the year 2000 climate state and integrate for 20 y with the emission scenarios fixed at the year 2000 level including GHGs and aerosols (59, 60). Emissions of aerosols and their precursors for the year 2000 were obtained from the Atmospheric Chemistry and Climate Model Intercomparison Project (59). In the perturbed simulations, the model configurations and parameters are the same as the *CTRL* simulations, except that we remove the major anthropogenic aerosol emissions including SO_2 and black carbon over China, referred to as *noCN* simulations. The aerosol-induced climate change can be obtained by subtracting the *noCN* from the *CTRL* ensemble averages. A slightly different perturbation in the initial atmospheric states is applied to each member to generate ensemble spreads. The statistical significances of the 500 hPa atmospheric temperature and SST responses among different ensemble members are evaluated with Student's *t* test at 90% and 95% confidence levels.

Data Materials, and Software Availability. All processed data to support the analysis and figure codes are available at https://doi.org/10.5281/zenodo.10648518 (61). The original observed and climate model data are publicly available online and can be downloaded from the following websites: ERSSTv5: https://psl.noaa.gov/data/gridded/data.noaa.ersst.v5.html; HadISST: http://www.metoffice.gov.uk/hadobs/hadisst/; COBE-SST2: https://psl.noaa.gov/data/gridded/data.cobe2.html; PDO index: https://www.ncei.noaa.gov/access/monitoring/pdo/; ERA5: https://www.ecmwf.int/en/forecasts/datasets/reanalysis-datasets/era5; CERES: https://ceres.larc.nasa.gov/data/; CO2 observation: http://scrippsco2.ucsd.edu/data/atmospheric_co2/primary_mlo_co2_record; CMIP5: https://esgf-node.llnl.gov/search/cmip5/; CMIP6: https://esgf-node.llnl.gov/search/cmip6/. The CESM2 code and scripts are publicly available online and can be downloaded from: https://www.cesm.ucar.edu/models/cesm2.

Author affiliations: [a]Key Laboratory of Physical Oceanography and Frontiers Science Center for Deep Ocean Multispheres and Earth System, College of Oceanic and Atmospheric Sciences, Ocean University of China, Qingdao 266100, China; [b]Laoshan Laboratory, Qingdao 266237, China; [c]Centre for Southern Hemisphere Oceans Research, Commonwealth Scientific and Industrial Research Organisation Oceans and Atmosphere, Hobart, TAS 7004, Australia; [d]Scripps Institution of Oceanography, University of California San Diego, La Jolla, CA 92093; [e]Max Planck Institute for Meteorology, Hamburg 20146, Germany; [f]National Oceanic and Atmospheric Administration/Geophysical Fluid Dynamics Laboratory, Princeton, NJ 08540; [g]University of Corporation for Atmospheric Research, Boulder, CO 80307; [h]School of Oceanography, Shanghai Jiao Tong University, Shanghai 200030, China; and [i]Southern Marine Science and Engineering Guangdong Laboratory (Zhuhai), Zhuhai 519082, China

1. T. Wernberg *et al.*, Climate-driven regime shift of a temperate marine ecosystem. *Science* **353**, 169–172 (2016).
2. T. L. Frölicher, C. Laufkötter, Emerging risks from marine heat waves. *Nat. Commun.* **9**, 1–4 (2018).
3. N. J. Holbrook *et al.*, Keeping pace with marine heatwaves. *Nat. Rev. Earth Environ.* **1**, 482–493 (2020).
4. D. A. Smale *et al.*, Marine heatwaves threaten global biodiversity and the provision of ecosystem services. *Nat. Clim. Chang.* **9**, 306–312 (2019).

5. J. A. Santora *et al.*, Habitat compression and ecosystem shifts as potential links between marine heatwave and record whale entanglements. *Nat. Commun.* **11**, 1–12 (2020).

6. R. M. McCabe *et al.*, An unprecedented coastwide toxic algal bloom linked to anomalous ocean conditions. *Geophys. Res. Lett.* **43**, 10–366 (2016).

7. K. E. Smith *et al.*, Socioeconomic impacts of marine heatwaves: Global issues and opportunities. *Science* **374**, eabj3593 (2021).

8. R. Seager *et al.*, Causes of the 2011–14 California drought. *J. Clim.* **28**, 6997–7024 (2015).

9. H. Shi *et al.*, Co-occurrence of California drought and Northeast Pacific marine heatwaves under climate change. *Geophys. Res. Lett.* **48**, e2021GL092765 (2021).

10. R. E. Howitt, J. Medellín-Azuara, D. MacEwan, J. R. Lund, D. A. Sumner, "Economic Analysis of the 2014 Drought for California Agriculture" (Center for Watershed Sciences, University of California-Davis, Davis, CA, 2014).

11. R. E. Howitt, D. MacEwan, J. Medellín-Azuara, J. R. Lund, D. A. Sumner, "Economic Analysis of the 2015 Drought for California Agriculture" (Center for Watershed Sciences, University of California-Davis, Davis, CA, 2015).

12. J. Medellín-Azuara, D. MacEwan, R. E. Howitt, D. A. Sumner, J. R. Lund, "Economic Analysis of the 2016 California Drought for Agriculture" (Center for Watershed Sciences, University of California-Davis, Davis, CA, 2016).

13. USDA Office of Communications, New Aerial Survey Identifies More than 100 Million Dead Trees in California, 18 November 2016. https://www.fs.usda.gov/about-agency/newsroom/releases/new-aerial-survey-identifies-more-100-million-dead-trees-california. Accessed 20 July 2023.

14. S. Baxter, S. Nigam, Key role of the North Pacific oscillation-West Pacific Pattern in generating the extreme 2013/14 North American winter. *J. Clim.* **28**, 8109–8117 (2015).

15. E. Di Lorenzo, N. Mantua, Multi-year persistence of the 2014/15 North Pacific marine heatwave. *Nat. Clim. Chang.* **6**, 1042–1047 (2016).

16. X. Ren, W. Liu, A. Capotondi, D. J. Amaya, N. J. Holbrook, The Pacific decadal oscillation modulated marine heatwaves in the Northeast Pacific during past decades. *Commun. Earth Environ.* **4**, 218 (2023).

17. N. A. Bond, M. F. Cronin, H. Freeland, N. Mantua, Causes and impacts of the 2014 warm anomaly in the NE Pacific. *Geophys. Res. Lett.* **42**, 3414–3420 (2015).

18. D. L. Hartmann, Pacific sea surface temperature and the winter of 2014. *Geophys. Res. Lett.* **42**, 1894–1902 (2015).

19. S. P. Xie, Westward propagation of latitudinal asymmetry in a coupled ocean-atmosphere model. *J. Atmos. Sci.* **53**, 3236–3250 (1996).

20. J. C. H. Chiang, D. J. Vimont, Analogous Pacific and Atlantic meridional modes of tropical atmosphere-ocean variability. *J. Clim.* **17**, 4143–4158 (2004).

21. M. A. Alexander *et al.*, The atmospheric bridge: The influence of ENSO teleconnections on air sea interaction over the global oceans. *J. Clim.* **15**, 2205–2231 (2002).

22. M. Newman, G. P. Compo, M. A. Alexander, ENSO-forced variability of the Pacific Decadal Oscillation. *J. Clim.* **16**, 3853–3857 (2003).

23. W. T. Hsiao, Y. T. Hwang, Y. J. Chen, S. M. Kang, The role of clouds in shaping tropical pacific response pattern to extratropical thermal forcing. *Geophys. Res. Lett.* **49**, e2022GL098023 (2022).

24. D. J. Amaya, A. J. Miller, S. P. Xie, Y. Kosaka, Physical drivers of the summer 2019 North Pacific marine heatwave. *Nat. Commun.* **11**, 1–9 (2020).

25. T. L. Frölicher, E. M. Fischer, N. Gruber, Marine heatwaves under global warming. *Nature* **560**, 360–364 (2018).

26. E. C. Oliver *et al.*, Projected marine heatwaves in the 21st century and the potential for ecological impact. *Front. Mar. Sci.* **6**, 734 (2019).

27. O. Boucher *et al.*, "Clouds and aerosols" in *Climate Change 2013: The Physical Science Basis. Contribution of Working Group I to the Fifth Assessment Report of the Intergovernmental Panel on Climate Change*, T. F. Stocker *et al.*, Eds. (Cambridge University Press, Cambridge, United Kingdom and New York, NY, 2013).

28. H. Wang, S. P. Xie, Q. Liu, Comparison of climate response to anthropogenic aerosol versus greenhouse gas forcing: Distinct patterns. *J. Clim.* **29**, 5175–5188 (2016).

29. D. M. Smith *et al.*, Role of volcanic and anthropogenic aerosols in the recent global surface warming slowdown. *Nat. Clim. Chang.* **6**, 936–940 (2016).

30. A. J. Dittus, E. Hawkins, J. I. Robson, D. M. Smith, L. J. Wilcox, Drivers of recent North Pacific decadal variability: The role of aerosol forcing. *Earth's Future* **9**, 1–14 (2021).

31. L. B. Kuntz, D. P. Schrag, Impact of Asian aerosol forcing on tropical Pacific circulation and the relationship to global temperature trends. *J. Geophys. Res. Atmos.* **121**, 14403–14413 (2016).

32. W. J. Dow, A. C. Maycock, M. Lofverstrom, C. J. Smith, The effect of anthropogenic aerosols on the aleutian low. *J. Clim.* **34**, 1725–1741 (2021).

33. B. Zheng *et al.*, Trends in China's anthropogenic emissions since 2010 as the consequence of clean air actions. *Atmos. Chem. Phys.* **18**, 14095–14111 (2018).

34. B. H. Samset, M. T. Lund, M. Bollasina, G. Myhre, L. Wilcox, Emerging Asian aerosol patterns. *Nat. Geosci.* **12**, 582–584 (2019).

35. L. J. Wilcox *et al.*, Accelerated increases in global and Asian summer monsoon precipitation from future aerosol reductions. *Atmos. Chem. Phys.* **20**, 11955–11977 (2020).

36. Y. Zheng, Q. Zhang, D. Tong, S. Davis, K. Caldeira, Climate effects of China's effort to improve its air quality. *Environ. Res. Lett.* **15**, 104052 (2020).

37. J. A. Johnstone, N. J. Mantua, Atmospheric controls on northeast Pacific temperature variability and change, 1900–2012. *Proc. Natl. Acad. Sci. U.S.A.* **111**, 14360–14365 (2014).

38. Z. Chen, J. Shi, C. Li, Two types of warm blobs in the Northeast Pacific and their potential effect on the El Niño. *Int. J. Climatol.* **41**, 2810–2827 (2021).

39. N. J. Mantua, R. H. Steven, The Pacific decadal oscillation. *J. Oceanogr.* **58**, 35–44 (2002).

40. C. Deser, M. A. Alexander, S. P. Xie, A. S. Phillips, Sea surface temperature variability: Patterns and mechanisms. *Ann. Rev. Mar. Sci.* **2**, 115–143 (2010).

41. Y. Joh, E. Di Lorenzo, Increasing coupling between NPGO and PDO leads to prolonged marine heatwaves in the Northeast Pacific. *Geophys. Res. Lett.* **44**, 11–663 (2017).

42. E. C. Oliver *et al.*, Longer and more frequent marine heatwaves over the past century. *Nat. Commun.* **9**, 1–12 (2018).

43. K. E. Taylor, R. J. Stouffer, G. A. Meehl, An overview of CMIP5 and the experiment design. *Bull. Am. Meteorol. Soc.* **93**, 485–498 (2012).

44. V. Eyring *et al.*, Overview of the Coupled Model Intercomparison Project Phase 6 (CMIP6) experimental design and organization. *Geosci. Model Dev.* **9**, 1937–1958 (2016).

45. C. Pascoe, B. N. Lawrence, E. Guilyardi, M. Juckes, K. E. Taylor, Documenting numerical experiments in support of the Coupled Model Intercomparison Project Phase 6 (CMIP6). *Geosci. Model Dev.* **13**, 2149–2167 (2020).

46. A. Lewinschal, A. M. Ekman, H. Körnich, The role of precipitation in aerosol-induced changes in northern hemisphere wintertime stationary waves. *Clim. Dyn.* **41**, 647–661 (2013).

47. G. Danabasoglu *et al.*, The Community Earth System Model Version 2 (CESM2). *J. Adv. Model.* **12**, e2019MS001916 (2020).

48. K. Caldeira, N. P. Myhrvold, Projections of the pace of warming following an abrupt increase in atmospheric carbon dioxide concentration. *Environ. Res. Lett.* **8**, 034039 (2013).

49. A. Barkhordarian, D. M. Nielsen, J. Baehr, Recent marine heatwaves in the North Pacific warming pool can be attributed to rising atmospheric levels of greenhouse gases. *Commun. Earth Environ.* **3**, 131 (2022).

50. S. Song, S. Yeh, H. Kim, N. J. Holbrook, Arctic warming contributes to increase in Northeast Pacific marine heatwave days over the past decades. *Commun. Earth Environ.* **4**, 25 (2023).

51. B. Huang *et al.*, Extended reconstructed sea surface temperature, version 5 (ERSSTv5): Upgrades, validations, and intercomparisons. *J. Clim.* **30**, 8179–8205 (2017).

52. N. A. A. Rayner *et al.*, Global analyses of sea surface temperature, sea ice, and night marine air temperature since the late nineteenth century. *J. Geophys. Res. Atmos.* **108**, D14 (2003).

53. S. Hirahara, M. Ishii, Y. Fukuda, Centennial-scale sea surface temperature analysis and its uncertainty. *J. Clim.* **27**, 57–75 (2014).

54. H. Hersbach *et al.*, The ERA5 global reanalysis. *Q. J. R. Meteorol. Soc.* **146**, 1999–2049 (2020).

55. S. Kato *et al.*, Improvements of top-of-atmosphere and surface irradiance computations with CALIPSO-, CloudSat-, and MODIS-derived cloud and aerosol properties. *J. Geophys. Res. Atmos.* **116**, D19 (2011).

56. C. D. Keeling *et al.*, Exchanges of atmospheric CO_2 and $^{13}CO_2$ with the terrestrial biosphere and oceans from 1978 to 2000. I. *Global Aspect*. (SIO Reference Series, No. 01-06, Scripps Institution of Oceanography, San Diego, CA, 2001), p. 88, http://escholarship.org/uc/item/09v319r9.

57. R. A. Plumb, On the three-dimensional propagation of stationary waves. *J. Atmos. Sci.* **42**, 217–229 (1985).

58. X. Liu *et al.*, Description and evaluation of a new four-mode version of the Modal Aerosol Module (MAM4) within version 5.3 of the Community Atmosphere Model. *Geosci. Model Dev.* **9**, 505–522 (2016).

59. J. F. Lamarque *et al.*, Historical (1850–2000) gridded anthropogenic and biomass burning emissions of reactive gases and aerosols: Methodology and application. *Atmos. Chem. Phys.* **10**, 7017–7039 (2010).

60. X. Liu *et al.*, Toward a minimal representation of aerosols in climate models: Description and evaluation in the community atmosphere model CAM5. *Geosci. Model Dev.* **5**, 709–739 (2012).

61. H. Wang, Data and Codes for PNAS: Atmosphere teleconnections from abatement of China aerosol emissions exacerbate Northeast Pacific warm blob events. *Zenodo*. https://doi.org/10.5281/zenodo.10648518. (30 January 2024).